PAPER

CrossMark
← click for updates

Synthesis, structural, magnetic and phase-transition studies of the ferromagnetic La₂CoMnO₆ double perovskite by symmetry-adapted modes

B. Orayech,*[a] I. Urcelay-Olabarria,[a,b] G. A. López,[c] O. Fabelo,[d] A. Faik[e] and J. M. Igartua[c]

A powdered La_2CoMnO_6 double perovskite was synthesized by the solid-state reaction method, and its crystal structure was investigated by (mode-crystallography) Rietveld analysis using X-ray and neutron powder diffraction data. La_2CoMnO_6 material is a monoclinic perovskite at room temperature, adopting the space group $P2_1/n$ ($a^-a^-b^+$), $a \approx b \approx \sqrt{2}a_p$, $c \approx 2a_p$ and $Z = 2$. The $P2_1/n$ phase can be described effectively by three distortion modes (GM_4^+, X_3^+, X_5^+) of the $Fm\bar{3}m$ ($a^0a^0a^0$) parent phase. The comparative study of the material and those in the Ln_2CoMnO_6 and Ln_2NiMnO_6 families has shown a general trend in nearly all the materials, has served to select a common direction in the sub-space spanned by X_5^+, tri-linearly coupled to the order parameters of the cubic to monoclinic first order phase transition. This direction has been used to parametrize the refinements and to perform reliable refinements in the high-temperature intermediate distorted trigonal phase, $R\bar{3}$ ($a^-a^-a^-$), for which only one effectively acting irrep has been deduced: GM_5^+, physically a tilt of the oxygen sharing octahedra of Co and Mn. Its temperature evolution up to the prototype cubic phase has been fitted in the framework of the Landau Theory of Phase Transitions, showing a behavior typical of a tricritical point. The low-temperature neutron powder diffraction data have served to solve the magnetic structure: three indistinguishable ferromagnetic models with the space groups $P2_1/n$ and $P2_1'/n'$ are proposed.

1 Introduction

Perovskites containing rare earth and transition metal cations on A and B sites exhibit interesting and useful electronic and magnetic properties. The double-perovskites Ln_2MMnO_6 are characterized by subtle structural distortions, caused by concerted rotations of the BO_6 octahedra and displacements of the A and B cations.

In the work of Dass *et al.* a series of $La_2CoMnO_{6-\delta}$ have been synthesized at different temperatures. All the samples treated at 1350 °C under air or oxygen flux could be indexed by the monoclinic $P2_1/n$ space group while the sample prepared at 600 °C, was poorly crystalline with a large anionic deficiency, refined within a pseudo-tetragonal model. Later the

same group studied La_2NiMnO_6 under different synthesis conditions. The structural analyses showed a random distribution of Ni and Mn over the octahedral sites occurring in the orthorhombic *Pbnm* and $R\bar{3}c$, while an ordering of Ni and Mn into distinguishable sites can be accommodated in $P2_1/n$ and $R\bar{3}$ (or $R\bar{3}m$).[1]

Bull *et al.* have proposed a monoclinic structure, with the space group $P2_1/n$, for La_2CoMnO_6 and La_2NiMnO_6 at room temperature. At high temperatures, a phase transition from the monoclinic $P2_1/n$ to the trigonal $R\bar{3}$ was observed for the first time in both compounds.[2] The study of Troyanchuk *et al.* on the $La_2CoMnO_{6.1}$ has shown the coexistence of two symmetries at room temperature: 75% of the orthorhombic phase *Pbnm* and 25% of the rhombohedral phase $R\bar{3}c$. While in the case of La_2CoMnO_6, a mixture of the *Pbnm* and $P2_1/n$ space groups was assigned. According to the authors, this coexistence is most likely associated with the inhomogeneous distribution of oxygen over a sample.[3] Some years later, the non-stoichiometric sample $Nd_2CoMnO_{6+\delta}$ was also investigated by Troyanchuk *et al.*, where an orthorhombic *Pbnm* symmetry was assigned to a random distribution of Co and Mn. The reduction to a stoichiometric compound ($\delta = 0$) has led to a large ionic ordering and therefore to lowering of the symmetry

[a]Departamento de Física de la Materia Condensada, Universidad del País Vasco, P.O. Box 644, Bilbao 48080, Spain. E-mail: brahim.orayech@ehu.es
[b]BCMaterials, Technological Park of Biscay, 48160 Derio, Spain
[c]Fisika Aplikatua II Saila, Zientzia eta Teknologia Fakultatea, Euskal Herriko Unibertsitatea, P.O. Box 644, Bilbao 48080, Spain
[d]Institut Laue-Langevin (ILL), 6 rue Jules Horowitz, BP156, 38042 Grenoble Cedex 9, France
[e]CICenergigune, Albert Einstein 48, 01510 Miñano, Alava, Spain

to a monoclinic structure $P2_1/n$.[4] Many reports started to appear on this family of materials, with a greater variety of cation-combinations. For instance, the series Ln_2NiMnO_6 (Pr, Nd, Sm, Gd, Tb, Dy, Ho and Y) has been studied by R. J. Booth *et al.*, where all the materials were indexed on monoclinic $P2_1/n$.[5]

Recently, two different samples of La_2CoMnO_6 have been prepared by A. J. Barón-González *et al*. The results have shown that the neutron powder diffraction data could be indexed in the monoclinic $P2_1/n$ with 97% and 73% of ordering over the B-site.[6] The monoclinic $P2_1/n$ has also been assigned for Lu_2CoMnO_6 with 97% of ordering[7] and for the crystals of Ln_2NiMnO_6 (Pr, Sm and Ho).[8] Despite this variety, from the structural point of view, reports concerning detailed determination of the structural phase-transitions of the La_2CoMnO_6 double perovskite type are very scarce. Only in Bull *et al.*'s work a phase-transition analysis has been reported for La_2CoMnO_6 and La_2NiMnO_6[2] where a phase transition from the monoclinic $P2_1/n$ to the trigonal $R\bar{3}$ has been observed.

In this work we analyze the synthesized very pure and well crystallized sample of La_2CoMnO_6. We have four goals. First, we would like to show the power of the use of mode-crystallography. In a first step it serves to focus clearly on the freedom the system adopts in the distorted structure of the prototype cubic. Secondly, it serves also, in the appropriate cases (as the one we report in this work), to parametrize the refinements. In particular, we focus our attention on the X_5^+ 3-dimensional irrep of the prototype $Fm\bar{3}m$ space group, and we explain how the parametrization is performed, this is the second goal. The third target of the report is to explain how the parametrization, deduced using reliable results from high-resolution neutron power diffraction data, can be securely used to refine data from other sources, like not high-resolution neutron diffraction data or X-ray powder diffraction. These last two targets are accomplished by performing a comparative analysis at room-temperature of some members of two families related to the reported materials: Ln_2CoMnO_6 and Ln_2NiMnO_6, a grand total of twelve structures taken from the literature have been analyzed, corresponding to eight different materials. Finally, we also report the magnetic structure and we show its thermal evolution.

The structures described in the present work $P2_1/n$, $R\bar{3}$ and $Fm\bar{3}m$ are in Glazer's notation $(a^-a^-b^+)$, $(a^-a^-a^-)$ and $(a^0a^0a^0)$, respectively.[9] That is the classical and usual notation used to refer to the possible distortions of the prototype high-symmetry phase. Howard and Stokes re-derived (and partly corrected) the Glazer's systems in terms of symmetry modes and in ref. 10, they specifically classified $A_2BB'X_6$ perovskites, amongst others.[11–15] We encourage the reader to follow the explanations given in ref. 10, specially sections 2.4 and 2.5, in which the authors derive the 12 tilting-only structures, amongst which those in the present work are included and on which the analysis we do is based, appearing when the R_1^+ ordering mode is combined with common − and + (Glazer's systems) modes R_4^+ and M_3^+ of the $Pm\bar{3}m$ prototype perovskite.

2 Experimental

2.1 Sample preparation

The La_2CoMnO_6 sample was synthesized by conventional solid state reaction. Stoichiometric ratios of $La(NO_3)_3·6H_2O$ (99.999%), $Co(NO_3)_2·6H_2O$ (99.999%) and $Mn(NO_3)_2·4H_2O$ (99.98%) were mixed in acetone medium and ground in an agate mortar. The mixed pink powder was subsequently heated in air at 420 K to remove the water. The resulting dark-brown residue was then ground and slowly calcined at 920 K for 24 h, at 1070 K for 24 h and at 1170 K for 48 h. The dark-brown powder was later ground, pressed to a pellet using a cold isostatic press and annealed in air at 1620 K for 24 h. After heating each time, the sample was cooled down slowly ($20\ K\ h^{-1}$) to ensure more complete absorption of oxygen by the lattice and reground to improve homogeneity. The synthesized sample was gray. X-ray diffraction measurements were performed after heating each time in order to control the quality of the obtained material.

2.2 Diffraction measurements and data analysis

Room temperature X-ray powder diffraction analysis was accomplished with a STOE STADI-P diffractometer equipped with a focusing germanium primary monochromator and a linear position-sensitive detector (PSD). The $CuK_{\alpha 1} = 1.5406$ Å wavelength was used. The data were collected in the range $20° < 2\theta < 120°$ with a step of 0.020° and a count-time of 600 s per step.

High-temperature X-ray powder diffraction data were collected on a Bruker D8 Advance diffractometer equipped with a primary germanium para-focusing monochromator and Bragg–Brentano geometry. The diffractometer is equipped with a Våntec high speed one-dimensional detector (with 3 angular apertures), using CuK_{α} radiation. An Anton Paar HTK2000 high-temperature chamber with a direct sample heating (Pt filament) and a temperature stability of 0.5 K was used. The specimens for high temperature measurements were prepared by mixing the material under study with acetone; the mixture was "painted" over the Pt-strip heater of the evacuated chamber. To determine the phase transitions and to obtain reliable values for the unit cell parameters in the whole temperature-range (300–1600 K), 47 diffraction patterns of 1 h measurement each were collected, with a temperature step of 25 K.

Neutron powder diffraction experiments were performed using the two-axis diffractometer D1B instrument at Institut Laue Langevin (Grenoble, France). The wavelengths used for the measurement were $\lambda_1 = 2.52$ Å and $\lambda_2 = 1.26$ Å with a ratio of 0.003. Approximately 2 g of the sample was placed in a vanadium can (6 mm) inside an "orange" LHe cryostat. Neutron diffractograms between 2 and 300 K, with a heating rate of 0.5 K min^{-1}, were collected using a detector with an angular coverage $0° < 2\theta < 128°$ and an angular resolution of 0.1°. LAMP software was used for data handling.[16]

The Rietveld refinement[17] of the structures was performed using FullProf. The peak shape was described by a pseudo-

Voigt function convoluted with axial divergence asymmetry function. The background level was modeled using selected points. The refined parameters were scale factor, zero shift, lattice constants, peak profile, asymmetry parameters, amplitudes of the modes transforming according to the irreps and independent isotropic atomic displacement parameters.

The input file for the Rietveld refinement was obtained by using the program AMPLIMODES for FullProf, located in the Bilbao Crystallographic server,[18,19] which has a module that prepares a pcr-file suitable for refining the data using the Win-Plotr/FullProf Package,[20] using symmetry-adapted modes instead of the usual approach that uses atomic coordinates.

2.3 Scanning electron microscopy (SEM)

Scanning electron microscopy (SEM) investigations were performed using a JEOL JSM6400 microscope with a W filament as an electron source and an Oxford PentaFETx3 energy-dispersive X-ray spectrometer (EDS) for elemental analysis. The accelerating voltage was 20 kV, and the beam current and the working distance for EDS analyses were 1 nA and 15 mm, respectively. The dead time during the analyses was in the range 20–35% and the live time for each measurement was 40 s. A standardless quantification was applied to determine the approximate composition of the sample. It can be assumed that the error for quantitative standardless EDS analyses is around 5%. To perform SEM analysis powders of the polycrystalline sample were placed on a graphite holder using double sided carbon tape and a graphite film of about 15 nm was deposited to make the sample conductive.

2.4 Transmission electron microscopy (TEM)

A Philips CM200 microscope equipped with a LaB_6 filament and a super-twin lens operating at 200 kV was used. Bright field images and electron diffraction patterns were acquired using a CCD camera (TVIPS GmbH). A Philips Be double-tilt holder was used to orient the sample. Powders of the sample for TEM characterization were dispersed in ethanol with ultrasound and drops were deposited on copper grids coated with amorphous carbon films. Electron diffraction patterns were simulated using the program JEMS (Stadelmann, 2004).[21]

3. Results and discussion

3.1 Overall morphology and characteristics of La_2CoMnO_6

The powder sample was investigated by SEM to analyze the overall appearance. Fig. 1a shows a bimodal distribution of, on the one hand, equi-axed particles ranging from about 2 up to 20 μm and, on the other hand, particles with a size smaller than 1 μm (see the inset in Fig. 1a). In addition, in the upper part of this inset, sharp edges of a sintered grain evidence the crystalline nature of the sample. Finally, the sample homogeneity can be observed in the back-scattered electron image shown in Fig. 1b. The contrast in these types of images is mainly generated due to the differences in the average atomic number for flat samples. In our case, since it is a powder sample, the different contrasts come only from the heights, but no impurities were detected.

3.2 Transmission electron microscopy at room temperature

Different particles of the powder sample were also investigated by TEM. Fig. 2a shows a bright field image of an electron transparent area of one particle; the contrast corresponding to
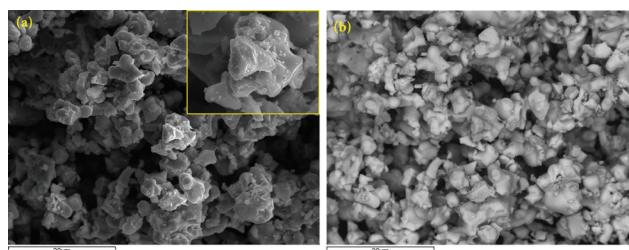
Fig. 1 (a) Secondary electron image showing the overall appearance of the powder sample. The inset shows an enlargement of a particle. (b) Back-scattered electron image showing the homogeneous character of the powder sample.
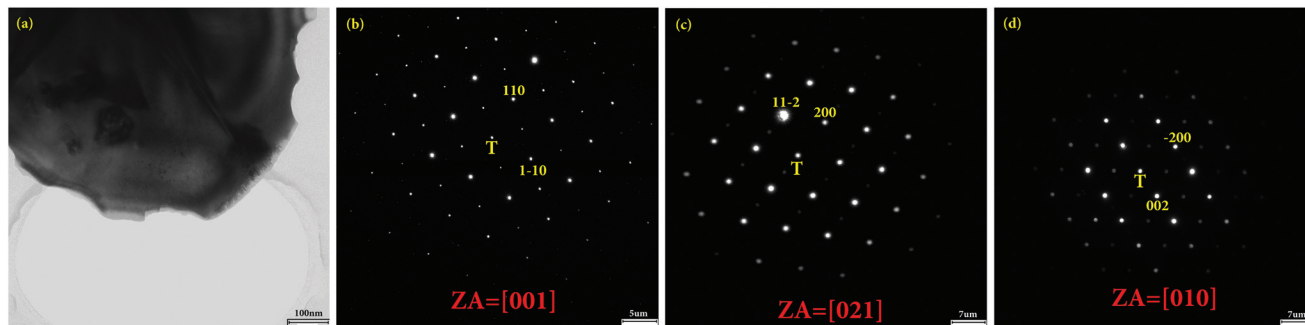
Fig. 2 (a) Bright field image of the electron transparent area of one particle. (b) Selected area electron diffraction pattern acquired along the [001] zone axis. (c, d) Electron microdiffraction pattern acquired along the [021] and [010] zone axis, respectively. The reflections indicated in the patterns were identified by simulations done with the JEMS software, using the neutron data.

small particles/fragments laying on the particle can be observed. Selected area and microdiffraction electron diffraction patterns were acquired after orienting the particle along different high-symmetry zone axes (ZA). The patterns shown in Fig. 2b–2d correspond well to those obtained from the theoretical simulations for the [001], [021] and [010] zone axes, respectively, using the crystallographic data (lattice parameters, space groups, atom positions and occupancy factors) determined from the XRD fitting described below. A full agreement between the electron diffraction investigation and the XRD data was observed.

3.3 Symmetry adapted mode-analysis of phases and phase-transition sequence

The refinement process has been done using the implementation of AMPLIMODES for FullProf, located in the Bilbao Crystallographic Server.[19] Our NPD data at room-temperature, recorded at the D1B instrument, are not the best ones for crystal-structure determination. On the one hand, the instrument is not a high-resolution one, and it is more suited for magnetic studies. On the other hand, it is also known that the material shows magnetic ordering,[22] starting at around 235 K. This is another remarkable point: even in this case, with low-resolution (for crystal structure) data and with magnetic response at low temperatures, the XRPD refinements, at higher

temperatures, will be improved, with the procedure we are proposing.

It is known, and the refinements also indicate it, the partial ordering of the Co and Mn cations over the two B- and B′-sites. It should be noted that it was not possible to fit the Co and Mn occupancies using the preliminary XRPD data (data we have at room temperature), due to the similarity in X-ray scattering factors between Mn and Co cations.[23,24] This is another reason for having collected NPD data.

Let us explain some aspects of the crystal structure procedure used for the refinements. For that, we need to know which are the irreps taking part in the distorted symmetry we are describing and what the symmetry-modes transforming according to those irreps physically do. We start with the structural symmetry at room temperature: $P2_1/n$ (ITA no. 14, non-standard setting).

The reported monoclinic structure and the reference one, the cubic parent phase (found using the program PSEUDO),[25,26] are listed in Table 1, which also shows the irreps taking part in the $Fm\bar{3}m \rightarrow P2_1/n$ symmetry breaking. There are seven irreps of the $Fm\bar{3}m$ space group taking part in the symmetry breaking: GM_1^+ (1), GM_3^+ (1), GM_4^+ (1), GM_5^+ (4), X_2^+ (1), X_3^+ (1), X_5^+ (3). There are 12 modes (one of them is the totally symmetric): 8(+1) modes move only the oxygen atoms in (24e) Wyckoff position and the remaining 3 modes move the A-site atoms in (8c).

Table 1 Input information for AMPLIMODES for FullProf: high-symmetry phase (prototype structure), low-symmetry structure information and transformation matrix. $P2_1/n$, $R\bar{3}$ (ITA no.148), and $Fm\bar{3}m$ (ITA no. 225). Second part of the table is a resume of the irreps taking part in the symmetry breaking from cubic $Fm\bar{3}m$ to the monoclinic $P2_1/n$ and $R\bar{3}$. The numbers in parenthesis indicate the number of modes transforming according to the irrep. The modes marked in bold character are the primary ones

High-symmetry structure: $Fm\bar{3}m$ $(a^0a^0a^0)$[9,10]
225
7.9200 7.9200 7.9200 90.00 90.00 90.00
4

Mn	1	4a	0	0	0
Co	1	4b	1/2	1/2	1/2
La	1	8c	1/4	1/4	1/4
O	1	24e	0.2471	0	0

Low-symmetry cell: $P2_1/n$ $(a^-a^-b^+)$[9,10]
014
5.5251 5.4875 7.7786 90 89.94 90
6

Mn	1	2a	0	0	0
Co	1	2b	0	0	1/2
La	1	4e	−0.0066	0.4645	0.7499
O	1	4e	−0.2771	0.2168	−0.0362
O	2	4e	−0.7982	0.2942	0.0400
O	3	4e	0.0753	0.0128	0.7580

Low-symmetry cell: $R\bar{3}$ $(a^-a^-a^-)$[9,10]
148
5.61494 5.61494 13.7096 90.0090.00 120.00
4

Mn	1	3a	0	0	0
Co	1	3b	0	0	1/2
La	1	6c	0	0	0.2467
O	1	18f	0.6645	0.8735	0.0781

Transformation matrix

$$\begin{pmatrix} 1/2 & 1/2 & 0 & | & 0 \\ -1/2 & 1/2 & 0 & | & 0 \\ 0 & 0 & 1 & | & 0 \end{pmatrix}$$

Transformation matrix

$$\begin{pmatrix} -1/2 & 0 & 1 & | & 0 \\ 1/2 & -1/2 & 1 & | & 0 \\ 0 & 1/2 & 1 & | & 0 \end{pmatrix}$$

$Fm\bar{3}m \rightarrow P2_1/n$

O1	24e	GM_1^+ (1) GM_3^+ (1) GM_4^+ (1) GM_5^+ (2) X_2^+ (1) X_3^+ (1) X_5^+ (2)
La1	8e	GM_5^+ (2) X_5^+ (1)

$Fm\bar{3}m \rightarrow R\bar{3}$

O1	24e	GM_1^+ (1) **GM_4^+ (1)** GM_5^+ (1)
La1	8e	GM_5^+ (1)

The GM_3^+ expands the octahedra in the equatorial *ab* plane, while the apical oxygens (in the *c* axis) are moved along the *c* axis to the center of the octahedra. GM_4^+ is essentially a rotation around the *b* axis; although it deforms a bit the octahedra (the displacement of the oxygens in the *ab* plane and the ones on the *c* axis is not the same). GM_5^+ is a four dimensional mode, actuating on A/A′-site cations and oxygens. Two of them displace the A/A′-site cations on *a* and *c* axes, respectively. The third one moves the equatorial oxygens in the *ab* plane, transforming in a rectangle the square formed by the equatorial oxygens, while the fourth is a kind of rotation along the *b* axis, with the apical oxygens displaced in the opposite direction of the rotation. The mode transforming according to X_3^+ is a pure rotation of the octahedra around the *c* axis; it acts only on the oxygen atoms of the *ab* plane. X_2^+ mode actuates on the equatorial oxygens, deforming into a rhombus the square formed by them. Finally, there is a three dimensional mode that transforms according to X_5^+. This mode actuates on the oxygens and on the A/A′-site cations. In the former case, it is a rotation around the *a* axis, although the amount of displacements in the *ac* plane and the ones on the *b* axis are not the same. In the latter, the A-site cations are displaced along the *b* axis.

From the Rietveld refinement results of La_2CoMnO_6, mode calculations of Ln_2MMnO_6 materials, shown in Table 2 and from the previous experience with related materials,[27–30] there are two active primary order parameters responsible for the cubic-to-monoclinic symmetry break, *i.e.* the monoclinic $P2_1/n$ is generated by two irreps of $Fm\bar{3}m$. The rest of the modes appears to be allowed by symmetry. Depending on the material, they could show different combinations of non-null mode amplitudes. But, in the double perovskite families usually there is only another irrep, the mode transforming according to X_5^+, that shows a non-so-negligible value for the mode-amplitude.

In summary, there are two active irreps (GM_4^+ and X_3^+), both represent physically tilts of the octahedra, and together with these, there is another non-negligible one, which is allowed by symmetry: X_5^+, in our experience, is always there. It has been proven to be tri-linearly coupled to the two main order parameters.[31] This is the physical origin to find non-converging refinements if one tries to nullify it in the refinements. Its values are always one order of magnitude smaller than the highest among the primary order parameters, *i.e.* GM_4^+, but being coupled, the refinements do not converge if it is excluded.

In relation to the refinement-process used, we have to mention also that, for the first temperature, at the beginning steps we have freed and refined all the mode-amplitudes, *i.e.* all the irreps, hence, all the degrees of freedom. Nevertheless, having seen the values for some of them and their corresponding associated errors, we have decided to nullify some. Hence, at the final step in the refinements, we have used only the following set of amplitudes, meaning that the final distorted structure is constructed using only those individual distortions: GM_4^+, X_3^+ and X_5^+.

Table 2 Refined values of the mode-amplitudes (in Å) taking part in the symmetry breaking from $Fm\bar{3}m$ to $P2_1/n$ (RT) for La_2CoMnO_6 in the present work [PW] with all modes freed and [PW*] with only the mode-amplitude (see the text): GM_4^+, X_3^+ and X_5^+. The results are compared to mode-amplitudes calculated for the materials in the Ln_2MMnO_6 family, which also show the same space group $P2_1/n$ at RT: La_2CoMnO_6,[2,6] Lu_2CoMnO_6,[41] Nd_2CoMnO_6,[42,43] La_2CoMnO_6,[42,43] Sm_2NiMnO_6,[5] Ho_2NiMnO_6,[46] Y_2NiMnO_6,[47] Tb_2NiMnO_6,[48]

| | | Amplitude | | | | | | | | | | | |
| | | La₂CoMnO₆ | | Lu₂CoMnO₆ | Nd₂CoMnO₆ | Ln₂NiMnO₆ | | | | | Y₂NiMnO₆ | Bi₂NiMnO₆ |
Irrep	Isotropy subgroup	[PW]	[PW*]	2	6	41	42	43	Ni[2]	Sm[5]	Ho[46]	Tb[5]	47	48
$Fm\bar{3}m \rightarrow P2_1/n$														
GM_1^+	$Fm\bar{3}m$(225)	0.004(11)	0.000	0.14(3)	0.17(2)	0.09(3)	0.11(2)	0.15(1)	0.05(4)	0.18(4)	0.09(2)	0.16(3)	0.15(3)	0.06(5)
GM_3^+	$I4/mmm$(139)	0.01(3)	0.000	0.03(3)	0.02(2)	0.05(3)	0.07(3)	0.19(7)	0.04(6)	0.25(4)	0.01(3)	0.02(3)	0.07(3)	0.02(5)
GM_4^+	$C2/m$ (12)	1.087(6)	1.080(3)	1.12(3)	1.10(2)	1.84(4)	1.32(3)	1.29(8)	0.73(5)	1.46(5)	1.70(3)	1.51(3)	1.65(3)	1.35(7)
GM_5^+	$C2/m$ (12)	0.14(4)	0.000	0.15(2)	0.10(2)	0.26(1)	0.12(2)	0.42(7)	0.61(2)	0.25(5)	0.21(1)	0.22(8)	0.21(1)	0.15(7)
X_2^+	$P4_2/mmm$ (136)	0.042(15)	0.000	0.07(3)	0.01(2)	0.09(3)	0.01(2)	0.04(7)	0.09(2)	0.02(5)	0.04(2)	0.12(3)	0.03(2)	0.01(6)
X_3^+	$P4/mnc$ (128)	0.523(6)	0.532(5)	0.53(3)	0.58(2)	1.31(3)	1.02(2)	0.96(7)	0.40(2)	0.83(5)	1.27(2)	1.06(3)	1.27(2)	0.68(6)
X_5^+	$Pmnn$ (58)	0.336(4)	0.334(3)	0.27(6)	0.27(5)	0.99(1)	0.60(6)	0.56(2)	0.71(2)	0.74(3)	0.88(1)	0.82(1)	0.90(1)	0.67(5)
Tolerance factor (t_{obs})		0.9477	0.9477	0.9437	0.9436	0.8546	0.8926	0.8976	0.9795	0.8893	0.8578	0.8586	0.9020	0.8596

K-vector: GM_1^+ (0,0,0), GM_3^+ (0,0,0), GM_4^+ (0,0,0), GM_5^+ (0,0,0), X_2^+ (0,1,0), X_3^+ (0,1,0), X_5^+ (0,1,0)
Direction: GM_1^+ (*a*), GM_3^+ (*a*,0), GM_4^+ (*a,a*,0), GM_5^+ (−*b,a,−a*), X_2^+ (0,*a*,0), X_3^+ (0,*a*,0), X_5^+ (*a,a*,0,0,*a,−a*)

We have refined the room-temperature NPD data. The idea is to find the best set, the best distribution, of the mode-amplitudes and use it for the subsequent refinements at high-temperatures and with XRPD data. The idea, also, is not to have the magnetic response when finding the best distribution. The

results of the refinements and the structural details at room temperature of the La_2CoMnO_6 are given in Tables 2–4 and Fig. 3a and b.

In Table 2 and in Fig. 4, we are showing the set of amplitudes resulting from the refined structures, at room-tempera-

Table 3 Structural details of La_2CoMnO_6 obtained at different temperatures from NPD (D1B, ILL) data using the $P2_1/n$ structural model freeing only the mode-amplitude (see the text): GM_4^+, X_3^+ and X_5^+. Mn/Co atoms occupy the site 2a (0, 0, 0), Co/Mn atoms occupy the site 2b (0, 0, 1/2), La atoms occupy the site 4e (x, y, z) and O atoms occupy the site 4e (x, y, z)

Temperatures		2 K	50 K	100 K	150 K	200 K	250 K	300 K
La	x	0.0000	0.0000	0.0000	0.0000	0.0000	0.0000	0.0000
	y	0.5213(3)	0.5218(3)	0.5229(2)	0.5222(2)	0.5215(2)	0.5206(3)	0.5211(3)
	z	0.2500	0.2500	0.25000	0.2500	0.2500	0.2500	0.2500
	B_{iso} (Å^2)	0.58(3)	0.58(3)	0.60(1)	0.71(1)	0.83(4)	0.88(1)	0.61(1)
O1	x	−0.7753(1)	−0.7748(7)	−0.7765(5)	−0.7740(5)	−0.7737(6)	−0.7739(6)	−0.7778(6)
	y	0.2757(1)	0.2752(7)	0.2735(5)	0.2733(5)	0.2736(6)	0.2726(6)	0.2697(6)
	z	0.0354(1)	0.0353(1)	0.0348(1)	0.0344(1)	0.0342(1)	0.0341(1)	0.0340(1)
	B_{iso} (Å^2)	0.61(1)	0.61(1)	0.68(3)	0.74(1)	0.78(2)	0.91(1)	0.82(2)
O2	x	−0.5709(2)	−0.5707(2)	−0.5696(16)	−0.5688(2)	−0.5684(2)	−0.5682(2)	−0.5681(2)
	y	0.5091(3)	0.5093(3)	0.5097(2)	0.5094(2)	0.5091(2)	0.5088(3)	0.5089(3)
	z	−0.2528	−0.2528	−0.2528	−0.2528	−0.2528	−0.2528	−0.2528
	B_{iso} (Å^2)	0.61(1)	0.61(1)	0.68(3)	0.74(1)	0.78(2)	0.91(1)	0.82(2)
O3	x	−0.2696(1)	−0.2691(7)	−0.2707(5)	−0.2683(5)	−0.2680(6)	−0.2682(6)	−0.2721(6)
	y	0.2186(1)	0.2191(7)	0.2208(5)	0.2210(5)	0.2207(6)	0.2217(6)	0.2246(6)
	z	−0.0354(1)	−0.0353(1)	−0.0348(1)	−0.0344(1)	−0.0342(1)	−0.0341(1)	−0.0340(1)
	B_{iso} (Å^2)	0.61(1)	0.61(1)	0.68(3)	0.74(1)	0.78(2)	0.91(1)	0.82(2)
Mn/Co	2a	0.28(1)/0.72(1)	0.28(1)/0.72(1)	0.28(1)/0.72(1)	0.28(1)/0.72(1)	0.28(1)/0.72(1)	0.28(1)/0.72(1)	0.28(1)/0.72(1)
Co/Mn	2b	0.72(1)/0.28(1)	0.72(1)/0.28(1)	0.72(1)/0.28(1)	0.72(1)/0.28(1)	0.72(1)/0.28(1)	0.72(1)/0.28(1)	0.72(1)/0.28(1)
Cell parameters	a (Å)	5.5029(1)	5.5034(1)	5.5048(2)	5.5065(1)	5.5084(1)	5.5112(1)	5.5128(1)
	b (Å)	5.4669(1)	5.4672(2)	5.4672(2)	5.4675(3)	5.4692(1)	5.4702(1)	5.4714(3)
	c (Å)	7.7435(1)	7.7438(1)	7.7431(8)	7.7456(1)	7.7473(5)	7.7493(1)	7.7526(1)
	β (°)	90.081(1)	90.053(1)	90.087(1)	90.081(1)	90.105(1)	90.135(1)	90.08(1)
	V (Å^3)	232.96(5)	233.00(1)	233.03(2)	233.19(1)	233.40(3)	233.62(1)	233.84(1)
Reliability factors	R_p (%)	2.75	2.63	2.25	2.14	2.18	2.33	1.57
	R_{wp} (%)	4.42	4.20	3.67	3.52	3.52	3.81	2.09
	R_{exp} (%)	0.85	1.13	0.85	1.13	1.13	1.13	0.90
	χ^2	5.2	5.8	5.2	5.71	5.67	4.2	5.32
	R_{Bragg}	4.5	5.1	4.01	4.67	5.10	3.5	4.89

Table 4 Main bond-distances (Å) for La_2CoMnO_6 obtained at different temperatures from NPD (D1B, ILL) data using the space group $P2_1/n$ (ITA no. 14, non-standard setting)

Temperatures Space group	300 K $P2_1/n$	250 K $P2_1/n$	200 K $P2_1/n$	150 K $P2_1/n$	100 K $P2_1/n$	50 K $P2_1/n$	2 K $P2_1/n$
CoO_6 octahedra							
Co–O1 × 2	1.944(3)	1.943(6)	1.943(5)	1.943(1)	1.944(1)	1.944(1)	1.944(3)
Co–O2 × 2	1.952(1)	1.951(7)	1.951(1)	1.951(2)	1.951(1)	1.952(3)	1.952(1)
Co–O3 × 2	1.947(2)	1.946(1)	1.946(2)	1.946(2)	1.946(1)	.946(4)	1.946(2)
Average distance	1.947(4)	1.947(1)	1.946(1)	1.947(1)	1.947(1)	1.947(2)	1.947(1)
Predicted distance	1.95	1.95	1.95	1.95	1.95	1.95	1.95
MnO_6 octahedra							
Mn–O1 × 2	1.991(3)	1.990(6)	1.990(1)	1.990(2)	1.990(2)	1.991(1)	1.9917(5)
Mn–O2 × 2	1.994(1)	1.994(1)	1.993(5)	1.993(4)	1.993(1)	1.995(7)	1.995(4)
Mn–O3 × 2	1.988(3)	1.987(4)	1.987(1)	1.987(3)	1.988(1)	1.988(4)	1.989(1)
Average distance	1.991(1)	1.990(1)	1.990(1)	1.990(1)	1.990(1)	1.991(1)	1.991(1)
Predicted distance	2.07	2.07	2.07	2.07	2.07	2.07	2.07
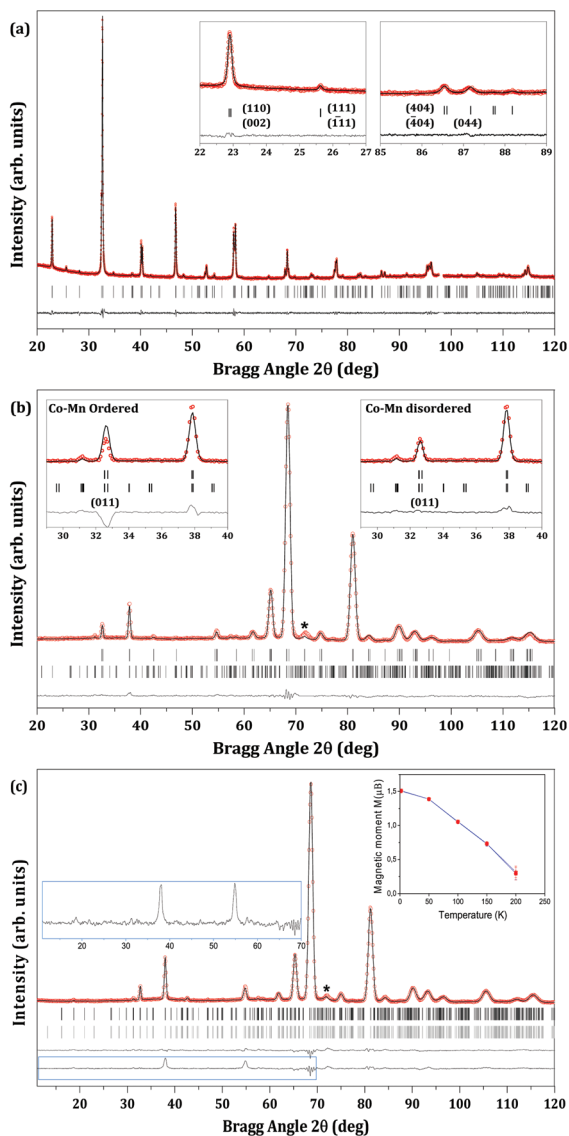
Fig. 3 Experimental (symbols) and calculated (line) (a) X-ray profiles and (b, c) neutron profiles from the Rietveld refinements of La$_2$CoMnO$_6$, using a structural model with $P2_1/n$ space group, (a) and (b) at room temperature, from XRPD data and NPD, respectively; and in (c) at 2 K, data from NPD. In (b) and (c), the (*)-symbol marked reflection corresponds to the signal of the vanadium sample container used in the experiment. The bars in the lower part of the graphics represent the Bragg reflection positions. In (b), the upper set of bars corresponds to the first wavelength λ_1 = 2.52 Å, and the lower set of bars corresponds to the second wavelength λ_2 = 1.26 Å. In (c), the upper set of bars corresponds to the nuclear structure reflections (for both wavelengths), and the lower set corresponds to the magnetic structure reflections. Insets show in detail (a): (22°–27°) the presence of the superlattice reflections of the form $h + k + l = 2n + 1$, corresponding to the $P2_1/n$ symmetry, (85°–89°) the cubic reflections (444) clearly splitted in the monoclinic symmetry into (044) (−404) (404), (b): selected region, (011) reflection, of the fitted results using an ordered and a disordered structural models. And (c): the upper difference curve refers to the refinement with both nuclear and magnetic structures, while the lower one was obtained from a refinement with only the nuclear structure (details shown in the inset) to show the isolated magnetic reflections. In panel (c) we are also showing in the right inset the evolution with temperature of the magnetic moments for the three proposed ferromagnetic models.
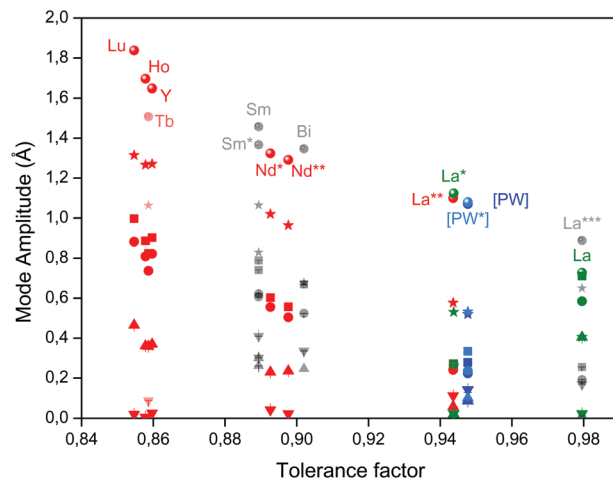
Fig. 4 Amplitudes of GM$_4^+$ (spheres), X$_3^+$ (stars), the global amplitude-value for the tri-dimensional X$_5^+$ irreps (squares) and their components: A10 (circles), A11 (up triangle) and A11 (down triangle), in the room-temperature structures of the Ln$_2$CoMnO$_6$ (Ln = La[PW], La*,[2] La**,[22] Lu[41] Nd*,[42] Nd**[43]), Ln$_2$NiMnO$_6$ (Ln = La,[2] La***,[44] Tb,[5] Sm,[5] Sm*,[45] Ho[46]), Y$_2$NiMnO$_6$[47] and Bi$_2$NiMnO$_6$[48] compounds, *versus* the tolerance factor values, calculated using bond distances. PW stands for present work: [PW] with all modes freed and [PW*] only the effectively acting ones, see the text.

ture, obtained for the materials of two families, Ln$_2$CoMnO$_6$ and Ln$_2$NiMnO$_6$, after having used the published structures as input to AMPLIMODES. The published structures included in this report have been refined by the authors using the conventional method: refining freely the 12 degrees-of-freedom, in the form of atomic co-ordinates. This means that when inputted to AMPLIMODES, all the mode-amplitudes have been the output. As mentioned before, the symmetry adapted mode-amplitude refinements naturally nullify some distortions, although they are permitted by symmetry.

In the first two columns of Table 2 with the resulting amplitude values, we show the results obtained for our material: firstly, having freed all the freedom, and then after seeing the values for some amplitudes, having freed only the effectively acting mode-amplitudes. Regarding the mode-amplitudes included in our refinements, it can be said that there are some materials not following the general trends observed for the mode-amplitudes transforming according to the GM$_4^+$, X$_3^+$ and X$_5^+$ irreps, as can be observed in Fig. 4: Tb (in red, dimmed), Sm and Bi (in black, dimmed). The Tb shows smaller values for the GM$_4^+$ and X$_3^+$ irreps than its counterparts for nearly the same tolerance factor. It also shows the same value for the global amplitude of the X$_5^+$ irrep, and nearly the same for the individual amplitudes in the internal sub-space. We have included two reports on the Sm material, and the results from both do not follow the trend. Although the values for GM$_4^+$ in both match the rest, and one of them reports a good value for X$_3^+$, the other values are systematically greater. This is also the case of the Bi material. On the other hand, in the same figure, we are showing some points in

green. Among those, the case of La_2NiMnO_6, with the highest tolerance factor seems to be pathological, for the two reports shown. The values of all the amplitudes of all the irreps are completely different from the rest. In green we have also shown another two studies on the same material we are reporting. The reason for showing them in green is clarified below.

We note that except for our material, the rest of the materials in both families show an unusual big value of the X_5^+ mode-amplitude. This value increases as the global distortion of the material, that is the structural distance from the actual crystal structure to the reference structure, increases as the tolerance factor diminishes. The high-limit for the distortion in the Co-family is Lu_2CoMnO_6. This fact plays in our favor, in the sense that the distortion being big it will be easier to be determined experimentally, as will be seen.

In subsequent paragraphs, we would like to focus our attention on the distortion transforming according to the X_5^+ irrep, because of the two reasons mentioned above: usually it shows a small value for the global amplitude of the mode and, on the other hand, it cannot be excluded from the refinement. The target of this analysis is to clarify if there is a preferable direction in this internal space which gives rise to a common type of partial distortion associated with the X_5^+ irrep, irrespective of the material in both families selected to accompany this report on La_2CoMnO_6.

The X_5^+ irrep is three-dimensional: there are three modes transforming according to it (Fig. 9 in ref. 28), two of which involve only oxygen atoms and the other one, only the A-site cation (La, in this case). In a previous paper,[32] based on the work reported in ref. 33, we have given enough experimental evidence of the fact that the polarization-vector, whose direction is equivalent to the direction of the generalized vector formed by the three amplitudes (the amplitudes taken as the components of the vector), maintains as the crystal structure evolves in the external field, temperature in this case, although its modulus decreases. The mentioned reports dealt with other materials, and other phases and irreps, but the concept is general. It is clear that the evolution should take place in the mentioned way, as the amplitudes represent the distortions of the reference structure: as the temperature increases, approaching to the prototype cubic phase, the distortion tends to decrease, but the relative variation of the amplitudes of the modes transforming according to the same irrep maintains. We have used this fact to perform a parametrized refinement: a set of three amplitudes has been described by just one parameter, arbitrarily chosen among the three (X_5^+, A10 in the jargon of FullProf, the mode-amplitude corresponding to the A-site cation, a translation of the cation along the y-axis (Fig. 9 in ref. 28)). The amplitudes of the other two have been fixed according to the following final direction: (0.95, −0.45, 0.00) (see below).

In our experience also, in some other related materials (ordered double perovskites),[28–30,49] this three-dimensional space reduces effectively to just a mono-dimensional one, since the relative importance of two of the three amplitudes is negli-

gible: their values actually go to zero (taking into account the errors), and, hence, they are taken out from the refinements. In this material, though, we have observed that two of them show a not null value, according to the data we have: A10 and A11, see discussion below. We have included the third one for completeness and to observe if its values remain so small in all the materials we want to compare.

In Fig. 5, we are showing the results only for the amplitudes of the 3-degenerate sub-space transforming according the X_5^+ irrep, at room-temperature. In panel (a), we are plotting in the xy plane the A11 amplitude, x-axis; and A12 amplitude, y-axis. The third amplitude, A10, is plotted in panel (b) of the same figure, at arbitrary fixed values on the x-axis, only for convenience, to separate in the same three sets and using the same color code, as in Fig. 4. The actual value of the component is indicated on the y-axis.

In panels (a) and (b), we are plotting three sets of arrows, in black, red and green color. For each colored set, we have two sub-sets: full color and dimmed. The dimmed color set of arrows represent the direction in the X_5^+ transforming three-dimensional sub-space, that results for each of the materials; that is, the direction of the polarization vector of this irrep. The full-color set of arrows is the actual vector representing the partial distortion induced by X_5^+; that is, the dimmed vector's amplitudes are multiplied by their corresponding global amplitude value, the total result gives the resulting distortion. In the case of the A10 amplitude, we are representing the actual values, a little bit to the right of their dimmed version, just for visualizing reasons. There is a blue arrow (dimmed and full-colored), which represents our structural data. To indicate the materials, we have labelled with arrows. The color-code used distinguishes three behaviors, as in Fig. 4: black arrows are defining a common direction, the red arrows another one, and the green arrows are the *outsiders*. We consider that these do not define a direction, with one exception, see below. We have discarded two of these three green results. Besides, we have grouped the heads of the black arrows, including the Tb red one, using an orange oval. All these materials have been studied using X-rays. The materials represented by red vectors have been studied using high-resolution ND (Ho, single-crystal diffraction and the rest, powder diffraction). Hence, we are discarding the results represented by the black arrows and we are assuming the red arrows to give the good (A11, A12) sub-distortion transforming according to X_5^+.

Not taking into account the Tb red arrow, there are 6 arrows, two of which, as indicated, correspond to two reports on the same material, Nd_2CoMnO_6. All these materials show an A12-amplitude absolute value very small (only Tb_2NiMnO_6 shows a negative A12 value), negligibly small: it vanishes if the error is taken into account. In view of this fact, we have assumed A12 to be actually zero. As a result, this gives an effective direction (c_1, c_2, 0.00) for the polarization vector, *i.e.* in the plane formed by the components (A10, A11), in the 3-dimensional sub-space transforming according to X_5^+. We show this effective direction in Fig. 5c, one arrow for each
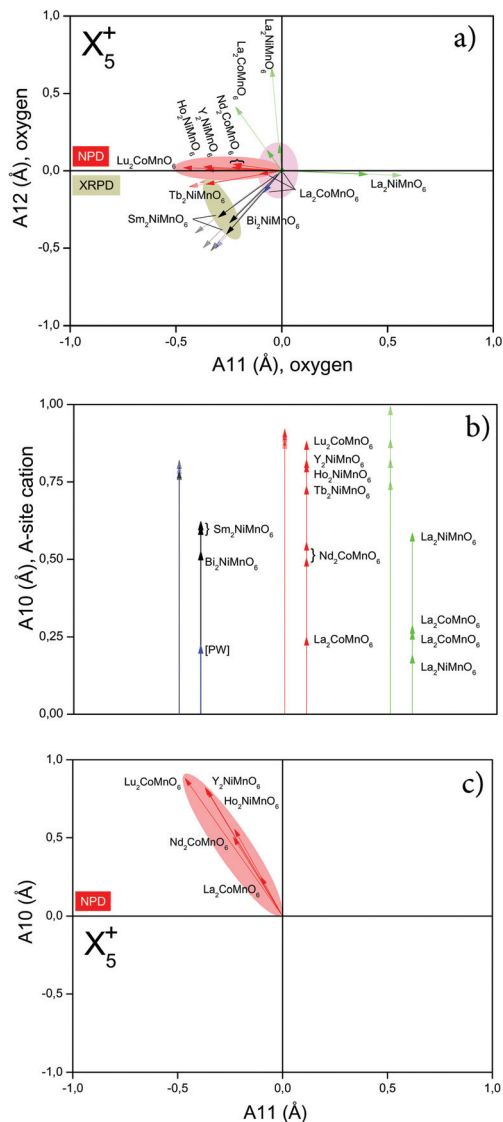
Fig. 5 (a) Two dimensional section, in the *x*-axis we show the A11 mode-amplitude and in the *y*-axis, the A12, of the three dimensional space transforming according to the X_5^+ irrep. The arrows represent a definite combination of those amplitudes deduced from the structures taken from the literature (as indicated), inputed in AMPLIMODES. Dimmed arrows represent the direction defined by the corresponding polarization vector. The full colored arrows indicate the actual distortion in this subspace (see the text). The color code reads as follows: red arrows represent structures proposed using NPD and assumed as good. Black are deduced using XRPD. The green color is used to indicate *outsiders*, except for the La$_2$NiMnO$_6$ NPD case. (b) Panel shows the third component of the X_5^+ irrep, A10. We are arbitrarily placing and separating the arrows for clarity reasons. (c) The final effective direction and the actual distortion in the reduced two-dimensional sub-space spanned by the modes A10 and A11. This is the direction used for the parametrization of the refinements.

material. The blue arrow corresponds to our material. As mentioned, our data are non-high-resolution NPD data.

There is an important remark on the green arrow representing materials: La$_2$NiMnO$_6$, which shows a positive A11 and a

negative (negligible small) A12. In fact, the vector is on the same direction as the red vector ones', but it is directed in the other sense. It is not difficult to show that both directions, considered the sense, represent equivalent structures, as they are associated, in the energy landscape, with two minima of the same depth. Hence, in fact, this green arrow actually is not an *outsider*, but, in contrast, represents a refined structure as the red vectors do, hence, equivalent to them. We have mentioned that this mode transforming according to X_5^+ is tri-linearly coupled to the two order-parameters: GM_4^+ and X_3^+. Thus, in a classical description of the phase-transition by the Landau Theory of phase transitions, there will be a term in the expansion of the free energy of the form: $cA_{GM_4^+} \times A_{X_3^+} \times A_{X_5^+}$ where c represents the intensity of the coupling and the *A*-factors represent the amplitude of mode transforming according the corresponding irrep. The order-parameters being blocked, any global change of sign in the sub-space spanned by the $(-|c2|, |c3|)$ (corresponding to the red vectors), will not change the sign of the coupling energy, which will give rise to an equivalent minimum. With the experimentally observed direction, restricted to the mentioned 2-dimensional sub-space, the only additional global sign-change corresponds to $(|c2|, -|c3|)$: nothing else but La$_2$NiMnO$_6$ in green. As mentioned, the distortion represented by this vector should be considered equivalent to the ones represented by the red vectors. Note that $(-|c2|, |c3|)$ is effectively $(-|c2|, \approx0)$.

Finally, in the same figure, panel (c), recovering the A10 component, we are plotting the effective direction $(|c1|, -|c2|)$ (vectors formed by A10 and A11 amplitudes, as we nulled the A12): the actual one used for the final parametrization of the refinements.

It is interesting to note that the inclusion of all the degrees of freedom of this irrep does not change too much the final result, being careful in this statement. The X_5^+ (A10) values do not change too much in the mentioned three refinements, although the vector itself is completely different, of course. The statement means that although the vector changes completely, the projection of that vector in the axes representing the A-site cation distortion (X_5^+, A10) does not change too much. Interesting to note also is the fact that even the vector changes quite a lot from one refinement to another (acquires components in the oxygen displacement sub-space, which physically represent a small tilt accompanied by a translation), the actual distortion is small.

The cell parameters of the corresponding materials at RT are shown in Fig. 6 *versus* the experimental tolerance factor. The materials are showing a similar behavior in a sense that the size and volume of the cell become larger as the tolerance factor increases, on the other hand the three cell parameters $\sqrt{2}a$, $\sqrt{2}b$ and c become closer as the size of the lanthanides placed on the A/A'-site becomes larger. In addition to that, even in the cell parameter evolution, the non-lanthanides Y$_2$NiMnO$_6$ and Bi$_2$NiMnO$_6$ follow perfectly the behavior shown by the lanthanide materials.

The refined structure at room-temperature was used as the starting point for the refinement at the lowest temperature
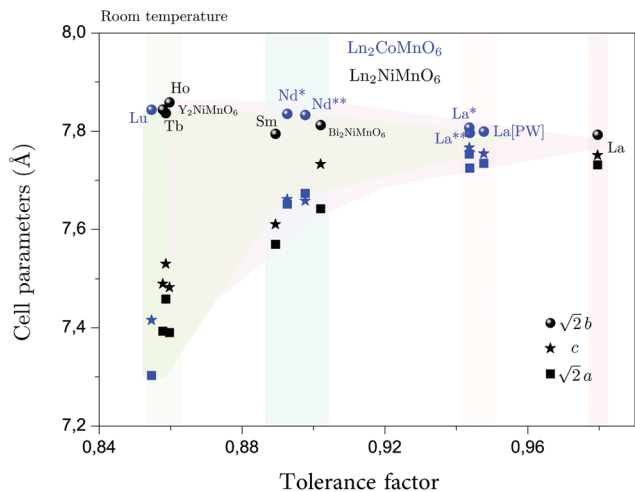
Fig. 6 Evolution, at room temperature, of the cell parameters along the analyzed structures in the families: Ln_2CoMnO_6 (blue) (Ln = La[PW], La*,[2] La**,[22] Lu[41] Nd*,[42] Nd**[43]); and, Ln_2NiMnO_6 (black) (Ln = La,[2] Tb,[5] Sm,[5] Ho[46]), Y_2NiMnO_6[47] and Bi_2NiMnO_6.[48] As in Fig. 4, we are using the experimental tolerance factor calculated using the experimentally obtained bond-distances. PW stands for present work.

tural details at 2 K of La_2CoMnO_6 are given in Table 3 and Fig. 3c.

The magnetic structure of La_2CoMnO_6 has been determined by means of neutron powder diffraction data collected in D1B at 2 K. The propagation vector is $\mathbf{k}$ = (000). The possible magnetic space groups are $P2_1/n$ and $P2'_1/n'$. As mentioned, from the crystal structure, it is known that the Co and Mn show disorder, in the two non-equivalent positions they occupy in the cell. It is also known that there is almost no magnetic contrast between Co and Mn. In this scenario, as the starting step for solving the magnetic structure, we have considered the amplitudes of the magnetic moments of the magnetic ions to be equal. Seeing the results from the refinements, we have constrained the sites to be equal, since the goodness of fit (gof) of the refinements does not vary.

Under all these considerations, there are three indistinguishable ferromagnetic models compatible with the data, with the magnetic moments along: y, 1.74(2) μ_B ($P2_1/n$ and 8.64), z, 1.75(2) μ_B ($P2'_1/n'$ and 8.67) and x, 1.74(2) μ_B ($P2_1/n$ and 8.97), the gof R-factors are given with the corresponding magnetic space group.

After having obtained the magnetic structure at 2 K, with the crystal structure being fixed, we freed the crystal structure, at the same temperature. Afterwards, we proceeded in the same way for the rest of the temperatures for which it is known the systems orders magnetically. In each case, we obtained the magnetic moment for the three mentioned possible magnetic models. The final results for the magnetic moments in the three equivalent models are plotted in the right inset of Fig. 3c. The results for the mode-amplitudes are shown in Fig. 8 (upper panel), with the rest of the values

without a magnetic response: 250 K. Knowing that there is no structural phase transition down to 2 K, to solve the magnetic structure we have taken that structure and fixed it at 2 K, as there is no crystal-symmetry change from room-temperature to 2 K. In this case, we would like to have the highest possible magnetic response to be more accurate in the magnetic structure refinement. The results of the refinements and the struc-

Fig. 7 Thermal evolution of selected ranges in 2θ, obtained from the XRPD experiment: (a) 24.5–27°, corresponding to the (111) primitive peak and (b) 56.5–60° presenting a clear region to follow the evolving of the intensity. (c) Represents the 66.5–69° 2θ interval corresponding to the (440) cubic reflections. In all the figures, the horizontal lines in white, a guide to the eye, show the transition temperatures. The other dashed lines, in black, are a guide to follow the disappearance of the splittings.

obtained for the amplitudes in the whole temperature range analyzed.

To investigate the phase transitions in the La_2CoMnO_6 compound at high temperatures, the structural thermal evolution was studied by laboratory X-ray diffraction measurements. Fig. 7(a–c) show the thermal evolution of the scattering intensity for three 2θ intervals in the temperature range from 300 K to 1600 K. A close analysis of the projected scattering intensity shows that the diffraction lines become closer to each other and the splitting reduces as the temperature increases, which is related to the fact that the unit cell distortion is less. Moreover, in Fig. 7a, the scattered intensity shows an abrupt discontinuous evolution of the characteristic reflections for the primitive unit cell, hkl with $h + k + l = 2n + 1$, which vanishes at 450 K. Hence, the cell transforms from the primitive monoclinic RT cell to another structure with a non-primitive cell, and higher symmetry. The observed phase transition has a discontinuous character, which can be clearly seen in Fig. 7b. This is very similar to what was observed in our previous studies for the antimony family: Sr_2LnSbO_6,[34] where this change was interpreted as evidence of the materials undergoing a discontinuous phase transition from the $P2_1/n$ space group to the trigonal phase $R\bar{3}$.

In addition to that, Bull *et al.* have reported that La_2CoMnO_6 shows a trigonal symmetry, $R\bar{3}$ space group, at 670 K.[2] Refinement attempts on the XRPD data above 450 K with the $R\bar{3}$ structure were successfully carried out. These results confirm the structural phase-transition character observed at 450 K: a first-order phase-transition from a monoclinic to a trigonal symmetry: $P2_1/n \rightarrow R\bar{3}$. There is no group–subgroup relationship between the monoclinic $P2_1/n$ and the trigonal $R\bar{3}$ and, thus, the experimentally observed phase transition should be of the first order, discontinuous, character which is the case. On the other hand, the intermediate trigonal phase $R\bar{3}$ will not be the reference structure of the RT phase. In the symmetry-mode analysis decomposition, the same virtual reference structure is used for the monoclinic and the trigonal space groups (see Table 1).

At higher temperatures, the XRPD data show that all the reflections become closer. For instance, the splittings of the reference cubic reflections 440 and 642 disappear continuously, as seen in Fig. 7c, and at about 1545 K the trigonal distortion of the unit cell disappears in a continuous way. This indicates the presence of a second phase transition from the intermediate trigonal symmetry to a higher symmetry one. The structural refinements of the patterns have confirmed that above 1545 K the structure can be described with the $Fm\bar{3}m$ space group.

This is the first time where both the trigonal-to-cubic phase-transition and the complete phase-transition sequence $P2_1/n \ (a^-a^-b^+) \rightarrow R\bar{3} \ (a^-a^-a^-) \rightarrow Fm\bar{3}m \ (a^0a^0a^0)$, is observed experimentally for La_2CoMnO_6. The same phase-transition sequence was observed in the case of several materials of the antimony family having a large size-difference among the Ln^{3+} and Sb^{5+} cations.[27,34–38] The temperature dependence of the amplitudes of the distortion-modes and the lattice
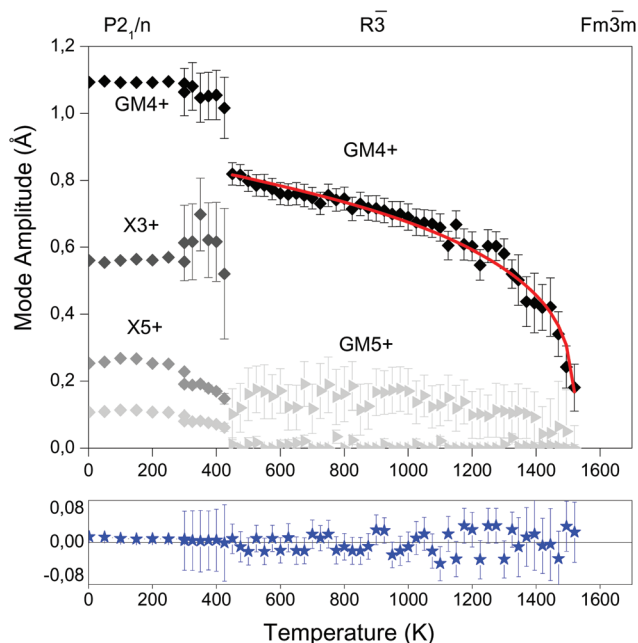
Fig. 8 Temperature evolution of the amplitudes of the modes breaking the symmetry from the cubic to the $P2_1/n$ and $R\bar{3}$ symmetries, as obtained from the NPD (2–300 K) and XRPD (300–1600 K) data refinements. The GM_4^+, X_3^+, X_5^+ ($P2_1/n$) and GM_4^+ ($R\bar{3}$) are the irreps of the symmetry-modes whose presence sets the distortions in the mentioned distorted phases. In the case of the X_5^+ irrep, in the low-temperature range, we are showing separately the effectively freed two components of the 3 dimensional sub-space the irrep spans. In the case of the $R\bar{3}$ space group symmetry, we are also showing, dimmed, the two components of the GM_5^+ irrep: they do not contribute effectively, so the final values of GM_4^+ for this symmetry correspond to them having been freed alone. The lower part of the graph (blue symbols) shows the relative difference in the whole temperature range between the GM_4^+ values in two refinements: only the effectively acting modes and all the modes freed. The continuous line in red is the fitting of the trigonal GM_4^+ amplitude values to the equation: $A_{GM_4^+} = A(0)_{GM_4^+}[T_c - T]^\alpha$, with the refined values $A(0)_{GM_4^+} = 0.127(8)$, $T_c = 1523(1)$ K and $\alpha = 0.26(1)$.

parameters, from 2 to 1600 K, are shown in Fig. 8 and 9, respectively.

For the trigonal $R\bar{3}$ phase, as shown in Table 1, there are three irreps that can take part in the symmetry breaking from the cubic ($Fm\bar{3}m$) to the trigonal $R\bar{3}$; GM_1^+ (1), GM_4^+ (1) and GM_5^+ (2), as usual, the number in parentheses indicates the number of modes transforming according to the corresponding irrep. The symmetry-mode decomposition performed by AMPLIMODES suggests that there is a single primary mode responsible for the symmetry breaking, the one marked in bold, which is the one transforming according to GM_4^+. The nullification of GM_1^+ and GM_5^+ did not affect the amplitudes of GM_4^+, the obtained results are plotted in the trigonal region, from 450 to 1600 K. It is worth noting the nearly continuous behavior, and decreases steadily the GM_4^+ amplitude value in $R\bar{3}$ symmetry. At the second phase-transition temperature, ≈1523 K, the GM_4^+ amplitude value goes to zero. In Fig. 8, and in the case of the $R\bar{3}$ space group symmetry, we are
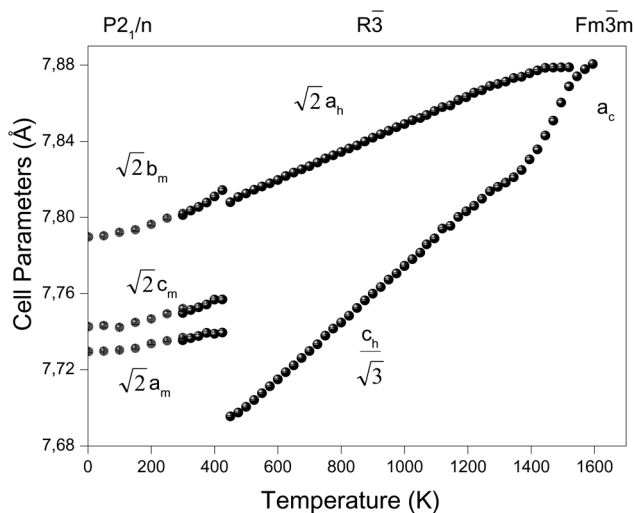
Fig. 9 Variation with temperature of the lattice parameters for La_2CoMnO_6, as obtained from the NPD (2–300 K) (dimmed black symbols) and XRPD (300–1600 K) data refinements. In the studied temperature range (2–1600 K), the compound undergoes two phase transitions: first-order one, discontinuous, at $\simeq$450 K transforming the cell from a monoclinic to a trigonal; and a second one of the second-order occurring at $\simeq$1520 K from a trigonal to a non-distorted cell, cubic. The phase-transition sequence is the following: $P2_1/n \rightarrow R\bar{3} \rightarrow Fm\bar{3}m$.

also showing, dimmed, the two components of the GM_5^+ irrep: they do not contribute effectively, as can be seen from their absolute values and/or their corresponding errors: they effectively nullify. Hence, the final values of GM_4^+ for this symmetry correspond to them having been freed alone. The lower part of the graph (blue symbols) shows the relative difference, in the whole temperature range, between the GM_4^+ values in two refinements: only the effectively acting modes and all the modes freed. As it can be seen, they are almost equal, except, perhaps, very near to the phase transition to the prototype cubic phase, where the underlying fluctuations give rise to higher errors in the determination of the structure.

Finally, the GM_4^+ amplitudes in this symmetry were perfectly fitted to the equation $A_{GM_4^+} = A(0)_{GM_4^+}[T_c - T]^\alpha$ where T_c is the critical temperature: the phase transition temperature. The fitting result values are $A(0)_{GM_4^+}$=0.127(8), T_c = 1523(2) K and α = 0.28(1). The exponent α value is very close to the Landau Theory prediction of 0.25 for a tri-critical transition. This behavior has also been observed and reported in some other cases, for instance in the $SrZrO_3$ simple perovskite.[39] This is an indication that the coefficient of the fourth power order parameter in the expression for the Gibbs free energy is negligibly small.[40]

4   Conclusions

We report the crystal structure at low- and high-temperatures and the magnetic structure of a highly pure and a well crystal-

lized sample of La_2CoMnO_6. We report the analysis of the structural phase transition sequence found for the material: $P2_1/n$ $(a^-a^-b^+)$ $\rightarrow$ $R\bar{3}$ $(a^-a^-a^-)$ $\rightarrow$ $Fm\bar{3}m$ $(a^0a^0a^0)$, from the lowest temperature for which we have data, neutron powder diffraction data at 2 K, up to 1600 K. For the first time the prototype cubic phase is reported experimentally. We also report the magnetic structure. We have considered the amplitudes of the magnetic moments of the magnetic ions to be equal and we have constrained the sites they occupy to be equal. We have found three indistinguishable ferromagnetic models compatible with the data, in the possible magnetic space groups: $P2_1/n$ and $P2'_1/n'$. We also report the thermal evolution of the magnetic moment.

Together with La_2CoMnO_6 we have analyzed the crystal structures at room-temperature of some members of two families related to it: Ln_2CoMnO_6 and Ln_2NiMnO_6. All the structural analysis has been done in the mode crystallography context. In this context, we report the perfect matching of the structural results on those materials analyzed using high-resolution NPD data obtained by refining the coordinates of the atoms as the structural degrees of freedom and our results refining only some of the symmetry allowed distortions. The system has chosen to free only the distortions transforming according to the irreps GM_4^+, X_3^+ and X_5^+. In particular, we have focused our attention in the 3 dimensional distortion subspace transforming according to the X_5^+ irrep. The analysis carried out in that space has permitted us to consider some of the literature results as confident and some others as not confident. We propose those to be re-visited. This analysis has also permitted us to define a direction, common to all the cases considered as good, as the direction in which the distortion associated with the irrep X_5^+ takes place: $(c1, c2, 0.00) \approx (0.920, -0.390, 0.00)$ are the components of the polarization vector. We have parametrized this direction, accordingly $(1.000, 0.424, 0.000)$, and we have used this parametrization to perform all the subsequent refinements, at low temperatures.

At high temperatures, the analysis carried out in the found trigonal intermediate distorted phase has shown that in this case there is only one irrep contributing effectively: GM_4^+. In this case also, the system does not use all the freedom it has when it distorts from the cubic prototype phase.

Acknowledgements

References

1 R. I. Dass and J. B. Goodenough, *Phys. Rev. B: Condens. Matter*, 2003, **67**, 014401.

2 C. L. Bull, D. Gleeson and K. S. Knight, *J. Phys.: Condens. Matter*, 2003, **15**, 4927.

3 I. O. Troyanchuk, A. P. Sazonov, H. Szymczak, D. M. Többens and H. Gamari-Seale, *J. Exp. Theor. Phys.*, 2004, **99**, 363–369.

4 A. P. Sazonov, I. O. Troyanchuk, V. V. Sikolenko, H. Szymczak and K. Bärner, *Phys. Status Solidi B*, 2007, **244**, 3367–3376.

5 R. J. Booth, R. Fillman, H. Whitaker, A. Nag, R. M. Tiwari, K. V. Ramanujachary, J. Gopalakrishnan and S. E. Lofland, *Mater. Res. Bull.*, 2009, **44**, 1559–1564.

6 A. J. Barón-González, C. Frontera, J. L. García-Muõz, B. Rivas-Murias and J. Blasco, *J. Phys.: Condens. Matter*, 2011, **23**, 496003.

7 S. Yañez Vilar, E. D. Mun, V. S. Zapf, B. G. Ueland, J. S. Gardner, J. D. Thompson, J. Singleton, M. Sánchez-Andújar, J. Mira, N. Biskup, M. A. Senaris-Rodriguez and C. D. Batista, *Phys. Rev. B: Condens. Matter*, 2011, **84**, 134427.

8 Z. Ganghua, L. Guobao, L. Fuhui, F. Yin, X. Ming and L. Jianhua, *J. Cryst. Growth*, 2011, **327**, 262–266.

9 A. M. Glazer, *Acta Crystallogr., Sect. B: Struct. Crystallogr. Cryst. Chem.*, 1972, **28**, 3384–3392.

10 C. J. Howard and H. T. Stokes, *Acta Crystallogr., Sect. A: Fundam. Crystallogr.*, 2005, **61**, 93–111.

11 C. J. Howard and H. T. Stokes, *Acta Crystallogr., Sect. B: Struct. Sci.*, 2004, **60**, 674–684.

12 C. J. Howard and H. T. Stokes, *Acta Crystallogr., Sect. B: Struct. Sci.*, 1998, **54**, 782–789.

13 H. T. Stokes, E. H. Kisi, D. M. Hatch and C. J. Howard, *Acta Crystallogr., Sect. B: Struct. Sci.*, 2002, **58**, 934–938.

14 B. J. Kennedy, C. J. Howard, K. S. Knight, Z. Zhang and Q. Zhou, *Acta Crystallogr., Sect. B: Struct. Sci.*, 2006, **62**, 537–546.

15 C. J. Howard, B. J. Kennedy and P. M. Woodward, *Acta Crystallogr., Sect. B: Struct. Sci.*, 2003, **59**, 463–471.

16 D. Richard, M. Ferrand and G. J. Kearley, *J. Neutron Res.*, 1996, **4**, 33–39.

17 H. Rietveld, *J. Appl. Crystallogr.*, 1969, **2**, 65.

18 M. I. Aroyo, J. M. Perez-Mato, D. Orobengoa, E. Tasci, G. de la Flor and A. Kirov, *Z. Kristallogr.*, 2011, **43**(2), 183–197.

19 D. Orobengoa, C. Capillas, M. I. Aroyo and J. M. Perez-Mato, *J. Appl. Crystallogr.*, 2009, **42**, 820–833.

20 J. Rodriguez-Carvajal, *Physica B*, 1993, **192**, 55–69.

21 P. Stadelmann, *JEMS. CIME-EPFL*, CH 1015 Lausanne, Switzerland, 2004.

22 A. J. Barón-González, C. Frontera, J. L. García-Muñoz, B. Rivas-Murias and J. Blasco, *J. Phys.: Condens. Matter*, 2011, **23**, 496003.

23 K. Asai, K. Fujiyoshi, N. Nishimori, Y. Satoh, Y. Kobayashi and M. Mizoguchi, *J. Phys. Soc. Jpn.*, 1998, **67**, 4218–4228.

24 T. I. Milenov, P. M. Rafailov, M. V. Abrashev, R. P. Nikolova, A. Nakatsuka, G. V. Avdeev, M. N. Veleva, S. Dobreva, L. Yankova and M. M. Gospodinov, *Mater. Sci. Eng., B*, 2010, **172**, 80–84.

25 E. Kroumova, M. I. Aroyo, J. M. Perez-Mato, S. Ivantchev, J. M. Igartua and H. Wondratschek, *J. Appl. Crystallogr.*, 2001, **34**, 783–784.

26 C. Capillas, E. S. Tasci, G. de la Flor, D. Orobengoa, J. M. Perez-Mato and M. I. Aroyo, *Z. Kristallogr.*, 2011, **226**(2), 477–485.

27 A. Faik, D. Orobengoa, E. Iturbe-Zabalo and J. M. Igartua, *J. Solid State Chem.*, 2012, **192**, 273–283.

28 E. Iturbe-Zabalo, J. M. Igartua, A. Faik, A. Larrañaga, M. Hoelzel and G. Cuello, *J. Solid State Chem.*, 2013, **198**, 24–38.

29 E. Iturbe-Zabalo, J. M. Igartua, A. Larrañaga, V. Pomjakushin, G. Castro and G. Cuello, *J. Phys.: Condens. Matter*, 2013, **25**, 205401.

30 E. Iturbe-Zabalo, J. M. Igartua and M. Gateshki, *J. Appl. Crystallogr.*, 2013, **46**, 1085–1093.

31 U. Petralanda and I. Etxebarria, *Phys. Rev. B: Condens. Matter*, 2014, **89**, 064107.

32 B. Orayech, A. Faik, G. A. López, O. Fabelo and J. M. Igartua, *J. Appl. Crystallogr.*, 2015, **48**, 318–333.

33 B. Kocsis, J. M. Perez-Mato, E. S. Tasci, G. de la Flor and M. I. Aroyo, *J. Appl. Crystallogr.*, 2014, **47**, 1165–1179.

34 A. Faik, E. Iturbe-Zabalo, I. Urcelay and J. M. Igartua, *J. Solid State Chem.*, 2009, **182**, 2656–2663.

35 A. Faik, M. Gateshki, J. M. Igartua, J. L. Pizarro, M. Insausti, R. Kaindl and A. Grzechnik, *J. Solid State Chem.*, 2008, **181**, 1759–1766.

36 A. Faik, J. M. Igartua, M. Gateshki and G. J. Cuello, *J. Solid State Chem.*, 2009, **182**, 1717–1725.

37 A. Faik, J. M. Igartua, E. Iturbe-Zabalo and G. J. Cuello, *J. Mol. Struct.*, 2010, **963**, 145–152.

38 A. Faik, I. Urcelay, E. Iturbe-Zabalo and J. M. Igartua, *J. Mol. Struct.*, 2010, **977**, 137–144.

39 B. J. Kennedy, C. J. Howard and B. C. Chakoumakos, *Phys. Rev. B: Condens. Matter*, 1999, **59**, 4023–4027.

40 E. K. H. Salje, Cambridge Topics in Mineral Physics and Chemistry, in *Phase Transitions in Ferroelastic and Co-elastic Crystals*, Cambridge University Press, The Pitt Building, Trumpington Street, Cambridge CB2 1RP, 1990, vol. 1.

41 S. Yáñez Vilar, E. D. Mun, V. S. Zapf, B. G. Ueland, J. S. Gardner, J. D. Thompson, J. Singleton, M. Sánchez-Andújar, J. Mira, N. Biskup, M. A. Señarís Rodríguez and C. D. Batista, *Phys. Rev. B: Condens. Matter*, 2011, **84**, 134427.

42 A. P. Sazonov, I. O. Troyanchuk, V. V. Sikolenko, H. Szymczak and K. Bärner, *Phys. Status Solidi B*, 2007, **244**, 3367–3376.

43 A. P. Sazonov, I. O. Troyanchuk, D. P. Kozlenko, A. M. Balagurov and V. V. Sikolenko, *J. Magn. Magn. Mater.*, 2006, **302**, 443–447.

44 W. Z. Yang, X. Q. Liu, Y. Q. Lin and X. M. Chen, *J. Appl. Phys.*, 2012, **111**, 084106.

45 W. Z. Yang, X. Q. Liu, H. J. Zhao, Y. Q. Lin and X. M. Chen, *J. Appl. Phys.*, 2012, **112**, 064104.

46 G. Zhang, G. Li, F. Liao, Y. Fu, M. Xiong and J. Lin, *J. Cryst. Growth*, 2011, **327**, 262–266.

47 M. Mouallem-Bahout, T. Roisnel, G. André, D. Gutierrez, C. Moure and O. Peña, *Solid State Commun.*, 2004, **129**, 255–260.

48 K. Takata, M. Azuma, Y. Shimakawa and M. Takano, *Funtai Oyobi Funmatsu Yakin*, 2005, **52**, 913–917.

49 B. Orayech, L. Ortega-San-Martin, I. Urcelay-Olabarria, L. Lezama, T. Rojo, M. I. Arriortua and J. M. Igartua, Structural phase transitions, Magnetic and Spectroscopic properties of the double perovskites $Sr_2Co_{1-x}Mg_xTeO_6$ (x = 0.1, 0.2 and 0.5), *Dalton Trans.*, 2015, DOI: 10.1039/C5DT02026C.